




Localized Reconnection Heating Inferred from the Three-dimensional Locations of Bright Active Region Coronal Loops

Dana Longcope¹, Marika McCarthy¹ , and Anna Malanushenko^{1,2}

¹ Department of Physics, Montana State University, Bozeman, MT 59717, USA; dana@solar.physics.montana.edu

² High Altitude Observatory, NCAR, P.O. Box 3000, Boulder, CO 80307, USA

Received 2020 May 19; revised 2020 August 3; accepted 2020 August 17; published 2020 October 5

Abstract

Coronal loops observed in soft X-rays and extreme ultraviolet imaging data offer direct evidence that coronal plasma is heated by some mechanism. That mechanism appears to energize a particular bundle of field lines somehow selected from the magnetized coronal volume. Magnetic reconnection localized to a patch within a coronal current sheet is one mechanism that would select a flux bundle at the same time it energized it. Since magnetic reconnection occurs preferentially at topological boundaries, we would expect to find coronal loops concentrated there if it were at work. We explore this hypothesis using a data set, previously compiled by McCarthy et al., consisting of 301 coronal loops interconnecting a pair of active regions over a 48 hr period. That work computed the three-dimensional geometries and magnetic field strengths for most of the loops. This revealed many bright loops lying at the periphery of the interconnecting flux domain, possibly created and energized by the reconnection that created the interconnecting flux. There were, however, many loops well inside the domain which would be difficult to attribute to that mode of reconnection. Here we use detailed magnetic models of the interconnecting domain to show that these internal loops tend to occur along internal boundaries: separatrices. This offers a novel form of evidence that coronal loops are the products of patchy reconnection even under quiescent conditions.

Unified Astronomy Thesaurus concepts: [Solar coronal loops \(1485\)](#)

1. Introduction

Coronal loops have presented several puzzles since they were first discovered (Vaiana et al. 1973; Rosner et al. 1978). They are narrow strands whose plasma density, higher than the surrounding corona, renders them visible in extreme ultraviolet (EUV) and soft X-rays, for lifetimes typically under 1 hr. Current thinking holds them to be bundles of magnetic field lines that have been selected from an otherwise volume-filling coronal magnetic field, and somehow energized. The energization mechanism might be the same one responsible for heating the corona in general—a mechanism that remains famously mysterious (see Klimchuk 2006, for an overview). Coronal loops may offer a constraint on the mechanism since, at least in their case, it appears to select a bundle of magnetic field lines out of a volume of presumably similar flux. A long-standing puzzle posed by their mere existence is how these flux bundles are selected and whether every field line in the active region’s (AR’s) coronal volume stands an equal chance of selection (Litwin & Rosner 1993).

Magnetic reconnection, one possible mechanism proposed to heat the corona (Galeev et al. 1981; Parker 1983; Heyvaerts & Priest 1984), is also an obvious candidate for selecting coronal loops (Beveridge et al. 2003). Reconnection appears more dramatically in solar flares where it is believed to rapidly convert stored magnetic energy into heat and other forms. Solar flares typically include an arcade of hundreds of distinct post-flare loops observed to brighten in various EUV bands over the course of the flare (Aschwanden & Alexander 2001). It has been proposed that a patchy reconnection process within the flare’s high-lying current sheet is responsible for both releasing the magnetic energy and producing the observed loops (Longcope et al. 2010, 2018; Qiu & Longcope 2016). Under that hypothesis the size and distribution of post-flare loops offers insight into the structure of the patchy flare reconnection

process (McKenzie & Savage 2011). One obstacle to interpreting this evidence is that the loops are formed far from their equilibrium configuration, during the very dynamic process of flare reconnection.

Reconnection has also been proposed as a means of heating the corona of quiescent ARs and of producing their coronal loops. Patchy reconnection at the coronal portion of a magnetic separator was proposed by Longcope et al. (2005) to explain coronal loops observed to interconnect an emerging AR with a nearby region. In a more recent study, McCarthy et al. (2019, hereafter Paper I) used 171 Å images from the Solar Dynamics Observatory/Atmospheric Imaging array (SDO/AIA; Lemen et al. 2012) to identify 301 coronal loops interconnecting an emerging region (AR 11149) to a nearby existing region (AR 11147) over the 48 hr period of emergence. The lifetimes of these loops (15 minutes median lifetime) suggested that they were observed in the process of cooling following their impulsive energization, possibly by reconnection.

Magnetic reconnection involves changes to field line topologies and is therefore closely associated with topological or geometrical boundaries in the magnetic field. Moreover, reconnection is believed to occur at current sheets that are themselves prone to form at these same boundaries. Genuine topological boundaries in a three-dimensional magnetic field include separatrices and their mutual intersections called separators (Hénoux & Somov 1987; Greene 1988; Lau & Finn 1990; Longcope 2005). There have been numerous studies of reconnection at these boundaries in general (Longcope 1996; Galsgaard & Priest 2000; Priest et al. 2005), in solar flares (Mandrini et al. 1991; Démoulin et al. 1993; van Driel-Gesztelyi et al. 1994; Bagalá et al. 1995; Longcope & Silva 1998) and under quiescent conditions (Longcope et al. 2001; Priest et al. 2002; Close et al. 2004; Tarr et al. 2014). In situations where such genuine topological boundaries are absent, current sheet formation and related reconnection have been identified with related *geometrical* structures known as quasi-separatrix layers

(QSLs; Priest & Démoulin 1995; Titov et al. 2002; Aulanier et al. 2005), where the field’s footpoint-to-footpoint mapping is strongly distorted but not actually discontinuous. In certain cases these geometrical structures can be related to separatrices through a limiting process (Démoulin et al. 1996; Titov & Hornig 2002). Separatrices and QSLs occupy only a small fraction of the coronal volume.

If current sheet reconnection were responsible for the selection and energization of quiescent AR loops, then it would seem to follow that only that flux near a topological boundary would have a chance of becoming a visible loop. The field lying well away from such boundaries would not undergo reconnection heating and would therefore never brighten as a loop. This suggests the possibility of testing the reconnection-selection hypothesis by mapping the field lines that appear as coronal loops and confirming their concentration along boundary layers and their absence from the interiors of topological domains.

The extensive loop catalog compiled by Paper I offers an unprecedented opportunity to pursue this strategy. In that investigation the authors used the method of Malanushenko et al. (2009) to combine the EUV loops with photospheric magnetograms from the Helioseismic and Magnetic Imager (HMI; Scherrer et al. 2012) in order to compute the three-dimensional structure of each loop. This three-dimensional map did reveal loops clustering along layers within the domain of reconnected flux (see Figure 13 of Paper I). They did not, however, develop a magnetic model detailed enough to identify these layers with topological magnetic boundaries. The aim of the present work is to take this important next step.

In one respect, the observations of Paper I would seem to support the view of coronal loops are formed by reconnection. The volume they studied consisted of flux that interconnected two different ARs, and was therefore necessarily the product of at least one reconnection event. This interpretation was, however, challenged by measurements of the magnetic flux in the collection of interconnecting loops. Paper I found that in total the observed loops accounted for more flux than could have been reconnected in order to simply join the two ARs. Indeed, the total flux exceeded that of either region alone. This excess was taken to be a signature of repeated reconnection energizing the interconnecting flux even after it had passed through the overlying separator to first become interconnecting flux. They suggested that this repeated reconnection occurred during process of Taylor relaxation to achieve a state of lower magnetic energy (Taylor 1974; Heyvaerts & Priest 1984; Nandy et al. 2003). The initial, or *external*, reconnection formed interconnecting flux, but subsequent *internal* reconnections occurred within the domain of interconnecting flux. The internal reconnection that Paper I ended up hypothesizing would constitute a coronal reconnection process both providing heat and forming distinct loops within the AR corona.

The present work returns to the measurements made in Paper I to explore in greater depth the process of reconnection, which may be both heating the corona and forming loops in and around ARs. That work found that most brightened loops were located inside the domain of interconnecting flux. It also noted that their distribution was not uniform, but rather that they tended to fall along a few surfaces, the insides of which were notably empty of bright loops. In the present work we use several more sophisticated magnetic models, including a nonlinear force-free field (NLFFF), to argue that the loops fall along separatrices internal to the interconnecting flux domain.

This provides further support for the hypothesis that magnetic reconnection both forms and heats coronal loops.

A bundle of field lines in an NLFFF will have a deformed cross section that can be circular, or nearly so, at only one place. We use our model to show that single place is more likely to be high in the corona than at one of its feet. The implication is that a process such as magnetic reconnection responsible for forming and energizing the loop must operate high in the corona. Taken together these loop properties provide new evidence supporting the hypothesis that coronal reconnection heats the quiescent solar corona.

We present and analyze this evidence as follows. The next section reviews the interconnecting loop observations from Paper I and the magnetic charge topology (MCT; see Longcope 2005, and references therein) model used in that work. It goes on to develop an MCT model of greater sophistication containing topological boundaries within the interconnecting domain. The interconnecting loops are found to lie near the internal boundaries of this model. Section 3 presents a new NLFFF that offers greater fidelity than the point source models. In this model as well, loops are found to lie along internal boundaries. The NLFFF model also shows how loop cross sections would vary along their lengths. From this we conclude that the circular portion of their cross section is more likely to be in the corona than at their feet. This finding argues in favor of magnetic reconnection operating higher in the corona. The final section discusses these lines of evidence and their implications.

2. Interconnecting Loops

Paper I sought to identify all coronal loops that formed to connect an emerging AR (AR 11149) to a nearby existing AR (AR 11147). Figure 1(d) shows seven of the loops found in the SDO/AIA 171 Å image (Figure 1(b)) interconnecting the ARs. A line of pixels, indicated by a horizontal magenta line and hereafter called the *dividing line*, was positioned between the emerging AR to its south and the existing AR to its north. Bright peaks within the pixel strip were used to identify interconnecting loops, such as those traced in red in Figure 1(d) and intersecting the dividing line at the green diamonds. The correspondence between a bright strip of pixels and an interconnecting loop was verified visually. In the end 301 interconnecting loops were found forming over the 48 hr emergence of AR 11149. The single instant shown in Figure 1, with seven loops, is typical of the full 48 hr series, with 301 loops. We will hereafter focus in-depth on this one time, and a window around it, under the assumption that it resembles most of the entire interacting period.

2.1. The Many-poles Magnetic Model

An MCT model of the AR pair was used to interpret the observed loops. Concentrations of photospheric flux in line of sight (LOS) HMI magnetograms were identified, after correcting for viewing angle, by grouping pixels with magnitude $|B_{\text{los}}| > 75$ G using the algorithm described in Barnes et al. (2005). For example, 53 flux concentrations were found in the magnetogram shown in Figure 1(a) (several centroids are denoted as black plusses and white crosses). Point magnetic charges were placed at the centroids on a tangent plane (the point of tangency $42''$ E, $462''$ N is indicated by the green asterisk on Figure 1(c)) and used to extrapolate a constant- α

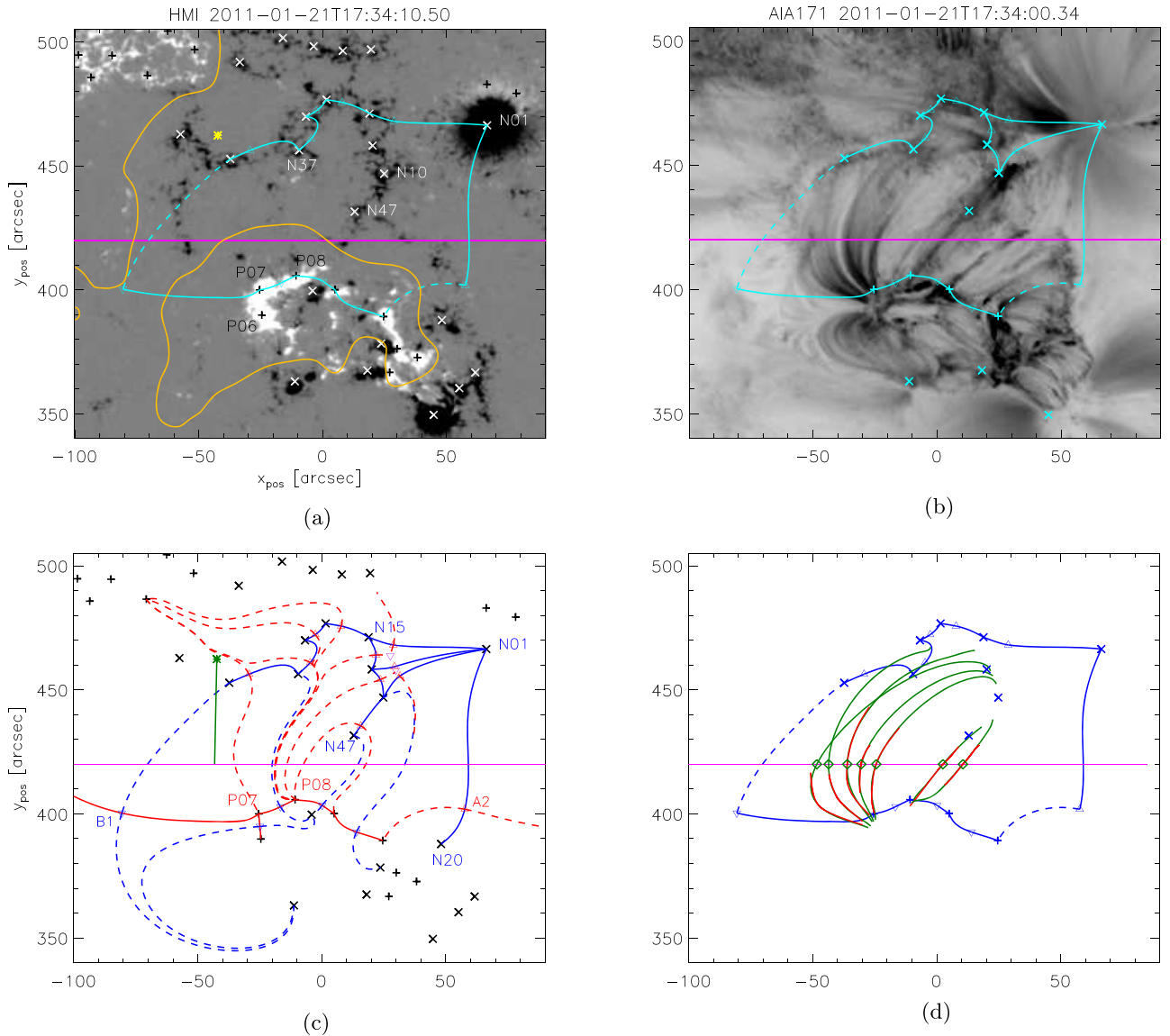


Figure 1. A subregion of the AR pair and its magnetic model at 17:34 on 2011 January 21. The dividing line appears in every panel as a horizontal magenta line separating the two ARs. (a) An HMI line of sight magnetogram in gray scale saturated at ± 500 G. Black plusses and white crosses show the centroids of photospheric flux concentrations, with several labeled. A set of topological curves shown in cyan connect some of the concentrations and approximately outlines the region of interconnecting flux. Orange curves follow the polarity inversion line (PIL) of a smoothed magnetogram. (b) SDO/AIA image at 171 Å from the same time shown in inverse, square-root gray scale. Several of the flux concentrations are shown in cyan, along with the interconnecting outline. (c) The skeleton of the MCT model extrapolated from point sources at the centroids (black plusses and crosses). Positive and negative null points are shown as red and blue triangles, respectively. Solid and dashed curves are spines and fan traces in the tangent plane. A green asterisk shows the point of tangency, connected by a line to the dividing line. (d) Seven coronal loops traced from the AIA image (b) are shown in red, and diamonds mark their intersection with the slit. Green curves show projections of three-dimensional magnetic field lines fit to the loops as described in Section 2.3.

force-free field. The field is given $\alpha = 5 \times 10^{-3} \text{ Mm}^{-1}$ approximating the median value found for the same time in Paper I. The field from each point charge is given by the Green’s function of Chiu & Hilton (1977), with that value of α . The MCT field from this set of 53 sources is called the *many-poles model*.

The topology of the many-poles magnetic field consists of numerous magnetic domains, distinguished by common point sources at the termini of their field lines. These domains are separated by fan surfaces, or separatrices, originating in the null points of the field (Priest et al. 1997; Longcope & Klapper 2002; Longcope 2005). The intersections of these surfaces with the tangent plane, composing the *skeleton footprint* of the field, are shown by red and blue curves in Figure 1(b), and the null

points in which they originate appear as triangles (Welsch & Longcope 1999). Domains intersecting this plane appear as regions bounded by solid or dashed curves (spines or fans, respectively). The domains crossing the dividing line compose the interconnecting flux. The perimeter of these domains is a subset of spine and fan field lines represented as a cyan or blue curves in all other panels of Figure 1. It is evident that those AIA loops (Figure 1(b)), which interconnect the new and old ARs, fall approximately within this perimeter, while loops entirely within AR 11149 lie outside it to the south.

At two corners of the perimeter are null points, labeled B1 and A2 in Figure 1(c). The fan surfaces from these null points combine to separate AR 11147 from AR 11149—i.e., old from new. The fan surface of the negative null point, A2, separates

flux originating in the main negative concentration of AR 11147, labeled *N01*, from flux originating in a small negative source in of 11149 labeled *N20*. Similarly, the positive null point *B1* separates flux originating in source *P07* of AR 11149, from flux originating in *P23* of 11147 lying far to the left of the cutout shown. Fan surfaces from these two corner nulls intersect the tangent plane along dashed portions of the cyan perimeter shown in Figure 1(a). The remainder of the perimeter consists of solid spine lines linking negative sources of AR 11147 (north) and positive sources of AR 11149 (south). Field lines between these linked sources form the entirety of the interconnecting flux.

2.2. The Quadrupole Model and the Dividing Plane

Paper I reduced the complicated many-poles MCT model described above to a far simpler quadrupole model. This was done by combining all sources of a given sign in a given AR into a single point source located at their collective centroid. This resulted in an MCT model with two sources for AR 11147 called P_o and N_o , and two for AR 11149 called P_n and N_n . The MCT field from these four sources, extrapolated using the same value $\alpha = 5 \times 10^{-3} \text{ Mm}^{-1}$, consists of four domains connecting the four sources in all possible ways.

The quadrupolar field has two null points, related to *B1* and *A2* of the many-poles model, and labeled in Figure 2(b). The fan surfaces from these null points form two separatrix surfaces dividing the volume into the four magnetic domains. Figure 2(a) shows the separatrix from null *B1* in perspective, rising above the tangent plane. Extending the dividing line along the LOS results in a plane, hereafter called the *dividing plane*, shown in perspective by a magenta rectangle in the figure. Because the point of tangency is north of disk center, the dividing plane makes an angle to vertical, leaning slightly toward the south. Any field line connecting between the ARs, including the fan surface of *B1*, must intersect the dividing plane. The intersection of the *B1* fan surface is shown on Figure 2(a) as a blue curve within the magenta rectangle: the dividing plane. That curve is then projected onto the vertical backplane and shown by a blue curve there on both Figures 2(a) and (b).

A second separatrix originates at the null *A2* (red triangle) but does not intersect the dividing plane within the volume depicted in Figure 2, and is therefore not plotted. The *A2* separatrix does intersect the *B1* separatrix along a curve called the separator (Baum & Bratenahl 1980; Longcope 2005), shown as an orange thick curve in Figure 2(a). Since it lies in both separatrices at once, and one (from *A2*) does not intersect the dividing plane, the separator does not intersect the dividing plane either.

New interconnecting field lines can only be created by reconnection across the separator curve (Greene 1988; Lau & Finn 1990). The integral of the reconnection electric field along the separator gives the rate that interconnecting flux is created, $\dot{\Phi}$ (Longcope 1996). If this reconnection provided the primary source of energy needed for bright coronal loops, then all observed loops would appear near the separator and thus near the separatrices. Since the separator does not cross the dividing plane, however, we would expect crossing loops to appear near the *B1* separatrix (i.e., the blue curve in Figure 2(b)). A census of such loops can be used to measure the flux that reconnected across the separator (Longcope et al. 2005).

Paper I sought to measure the reconnection electric field along the separator by identifying all the interconnecting flux at the instant it was created. A tacit assumption of this approach is that interconnecting flux will brighten only once, when it is first reconnected across the separator. Interconnecting flux is guaranteed to have undergone this one reconnection, but it is possible for it to reconnect again, to other interconnecting flux.

Examples of seven interconnecting loops that cross the dividing plane are shown in Figures 1(b) and 2(b). Paper I identified 301 such loops over the 48 hr emergence of AR 11149 in order to quantify the reconnection. They found that the accumulated magnetic flux in all these loops accounted for more flux than could be in the interconnecting domain—it was more flux than in the emerging AR itself. The authors ultimately concluded that some energization process different from the separator reconnection described above was responsible for the loops. This energization caused interconnecting flux to brighten several times, leading to an overestimation of reconnected flux. One possibility raised by Paper I was that after reconnecting across the *B1*–*A2* separator to form interconnecting flux, field lines reconnected across separators internal to the interconnecting domain.

2.3. Modeling Observed Loops in Three Dimensions

In an effort to better understand the reconnection and loop brightening, each loop observed in EUV was used to compute a coronal field line in three dimensions. Tracing a loop on the AIA 171 Å image, as done in Figures 1(b) and (d), provides the projection of a field line onto the plane of the sky (PoS). The point the loop crosses the dividing line, shown as a green diamond on Figure 1(d), represents an entire line within the dividing plane—a line parallel to the LOS. The actual field line must intersect this straight line at some unknown height h above the photosphere. Following the method first proposed in Malanushenko et al. (2009), Paper I computed a number of possible field lines by initializing them at points of different heights h . The field lines were traced through a linear force-free field (LFFF) extrapolated into a rectilinear volume from a portion of the HMI LOS magnetogram (i.e., not the point source approximation) placed along the bottom boundary. The LFFFs are calculated via convolution of the lower boundary (HMI magnetogram) with an unbounded Green’s function (Chiu & Hilton 1977), so the resulting field has no lateral or upper boundaries.

After being traced in both directions from initial point h , the field line was projected back to the PoS and quantitatively compared to the traced AIA loop using a discrepancy integral. The procedure was repeated for a range of initial positions h using a number of extrapolations with values of α covering a range including $\alpha = 0$ (see Malanushenko et al. 2009, for details of this fitting method). The field line that yields the minimum discrepancy, from all values of h and α , is deemed to be the one corresponding to the observed loop. The end result is a three-dimensional curve, the magnetic field strength along that curve, and a value of α , for each observed coronal loop. This procedure, hereafter called α - h fitting, was repeated for most of the interconnecting loops observed in AIA 171 Å leading to a set of 199 three-dimensional field lines over the 48 hr observation (Paper I).

The three-dimensional loops found through α - h fitting formed the basis of the investigation in Paper I and were used as part of the descriptions in previous sections of this work. A

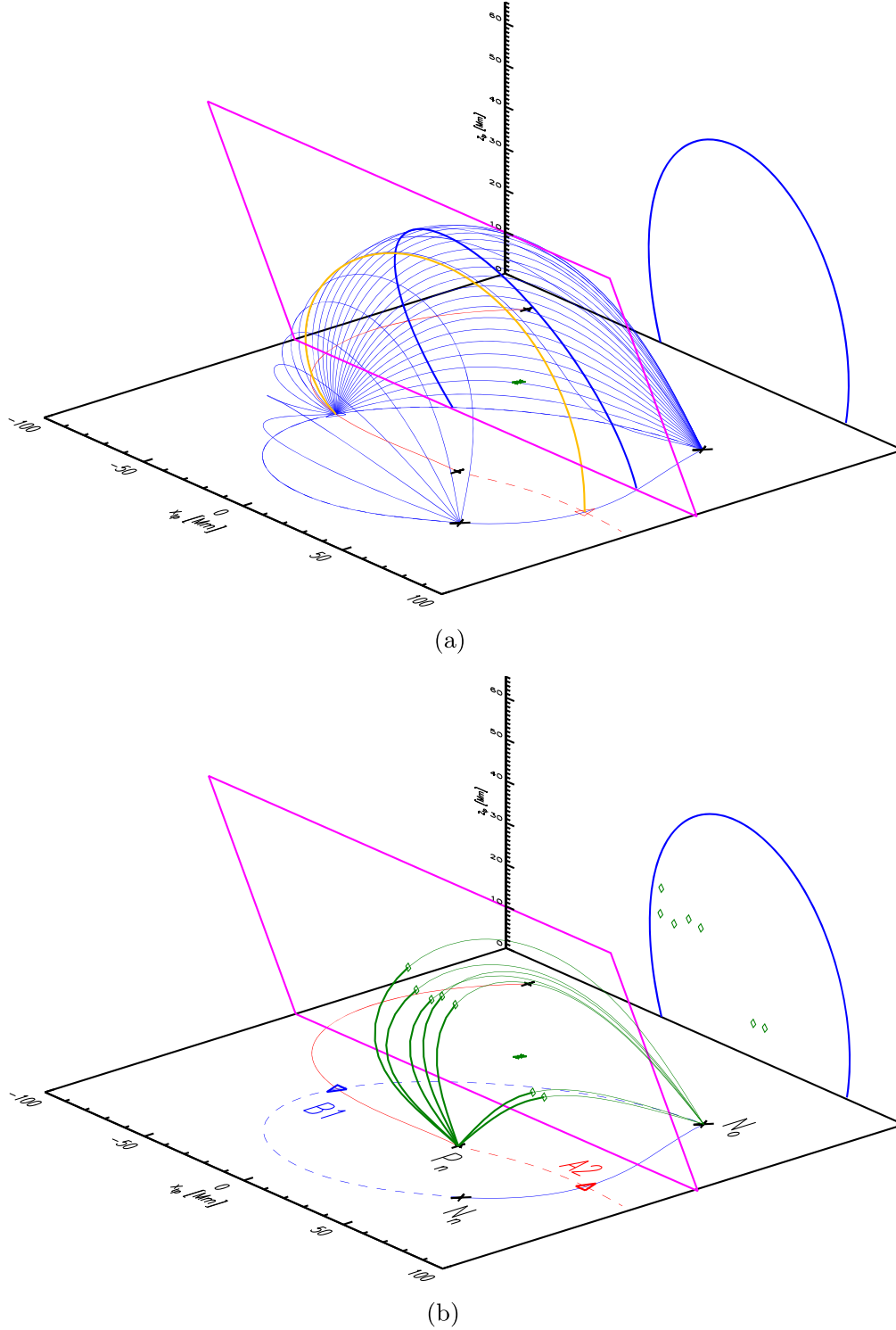


Figure 2. Perspective renderings of the quadrupole field model. A section of the tangent plane forms a black rectangle along the bottom, on which the four sources are marked by black plusses and crosses, null points by red and blue triangles, and the point of tangency by a green asterisk. The vertical z coordinate rises from one corner of the tangent-plane rectangle. Magenta lines outline a section of the dividing plane. (a) The separatrix curve from $B1$ is indicated by a number of thin blue field lines originating from the null (blue triangle) and ending at either of the negative sources (black crosses). The intersection of this surface with the dividing plane is shown by a thick blue curve in perspective. This is projected onto the back vertical plane to form another blue curve. The separator, shown as an orange thick curve, lies in the separatrix surface, but connects null $B1$ to null $A2$. (b) Seven field lines (green curves) cross the dividing plane at the seven green diamonds. These intersections are projected onto the backplane where they appear as green diamonds underneath the projection of the separatrix intersection (blue). The two null points and three of the point sources are labeled.

loop's contribution to the interconnecting flux was computed by multiplying the area of its cross section at the dividing plane by its field strength there. The cross section was assumed to be

circular with a diameter given by the FWHM, background-subtracted brightness of the peak in the strip of AIA pixels. The value $\alpha = 5 \times 10^{-3} \text{ Mm}^{-1}$, used for the MCT, was taken from

the median of the values from the α - h fits around at 17:34 on 2011 January 21. Finally, the positions at which the seven loops observed at that time crossed the dividing plane are depicted by the green diamonds on Figure 2(b).

The three-dimensional view thus obtained corroborated the suspicion that loops were being brightened at times other than the reconnection that first introduced them to the interconnecting domain. Most of the green diamonds on Figure 2 appear well inside the separatrix surface. To see this, compare their location in the projection plane to the blue curve, which is the projection of the $B1$ separatrix. All interconnecting flux must cross the dividing plane underneath the blue curve and all seven field lines do so. Furthermore, all seven field lines in this quadrupolar MCT connect between sources P_n and N_o . A field line that has recently undergone reconnection would, however, be near the domain's outer boundary and intersect the dividing plane in the vicinity of the blue curve. Many of the green diamonds are rather far inside; two are very low down and well inside. It seems very unlikely that these low-lying curves were energized by reconnection across the quadrupolar separator.

Paper I concluded that many of the observed loops were brightened by reconnection *internal to the interconnecting domain*. The quadrupolar model lumps all footpoints from a given AR into a single source. The positive polarity of 11149, for example, is represented in the quadrupole model by a single point source, P_n . In contrast, the many-poles model uses numerous different sources to represent this polarity: Figure 1 calls out $P06$, $P07$, and $P08$. The exchange of footpoints between $P06$ and $P07$ is reconnection internal to the AR 11149 and thus not captured in the quadrupole model.

2.4. Reconnection in the Many-poles Model

In order to account for internal reconnection, we must abandon the simplified quadrupole model and return to the more complicated many-poles model. Figure 3(a) shows the skeleton of the many-poles model through its intersections with the tangent plane (bottom black rectangle) and the dividing plane (tilted magenta rectangle) in a perspective view similar to Figure 2(b).

The skeleton of the many-poles model is naturally more complicated than that of the quadrupole model. Both models include a single null point, labeled $B1$ in both cases, whose fan surface separates flux of the positive polarity of AR 11147 from flux from the positive polarity of AR 11149. The many-poles model includes separatrices and separators absent from the quadrupole model. All the red curves and all but the uppermost blue curve on Figure 3(b) are internal separatrices.

The proximity of the green diamonds to internal negative (red) separatrices supports the hypothesis that reconnection internal to the interconnecting domain is responsible for reenergizing these loops. Five of these are reasonably close to a coronal spine line. The lowest two fall near the separatrix separating flux from $N10$ from flux from $N47$.

The many-poles model has proven useful in understanding the nature of the interconnecting flux and how internal reconnection may be powering the observed loops. While providing clarity, the model suffers from several drawbacks which compromise its utility in precisely locating reconnection. The first inaccuracy is that it is an LFFF model using a single value of α . The actual coronal field is almost certainly an NLFFF, with $\alpha(\mathbf{x})$ varying over the volume. Indeed, α - h fitting of the 199 different loops reveals a range of different α values. The second source of

inaccuracy is that by its nature the MCT model is extrapolated from point sources rather than a continuous distribution of photospheric field, as the HMI measurement in Figure 1(a) shows. Both of these inaccuracies will be mitigated by using the NLFFF described in the next section.

3. The NLFFF

An NLFFF should provide a more accurate magnetic model with which to interpret loop locations. The most common method for constructing an NLFFF is to use a vector magnetogram made at the photosphere and extrapolate upward into the corona (see De Rosa et al. 2009 for a discussion of different methods and their comparison). Doing so, however, disregards all the information already gained from the EUV loops about the coronal field. This information is central to our study, so it makes more sense to use it in the construction of the NLFFF, than to discard it in favor of additional photospheric magnetic measurements. We therefore opt to use the HMI magnetograms along with the EUV loops observed by SDO/AIA 171 Å in the quasi-Grad-Rubin (QGR) method of Malanushenko et al. (2012). This method yields an NLFFF throughout the full coronal volume, which matches the magnetogram across its entire lower boundary.

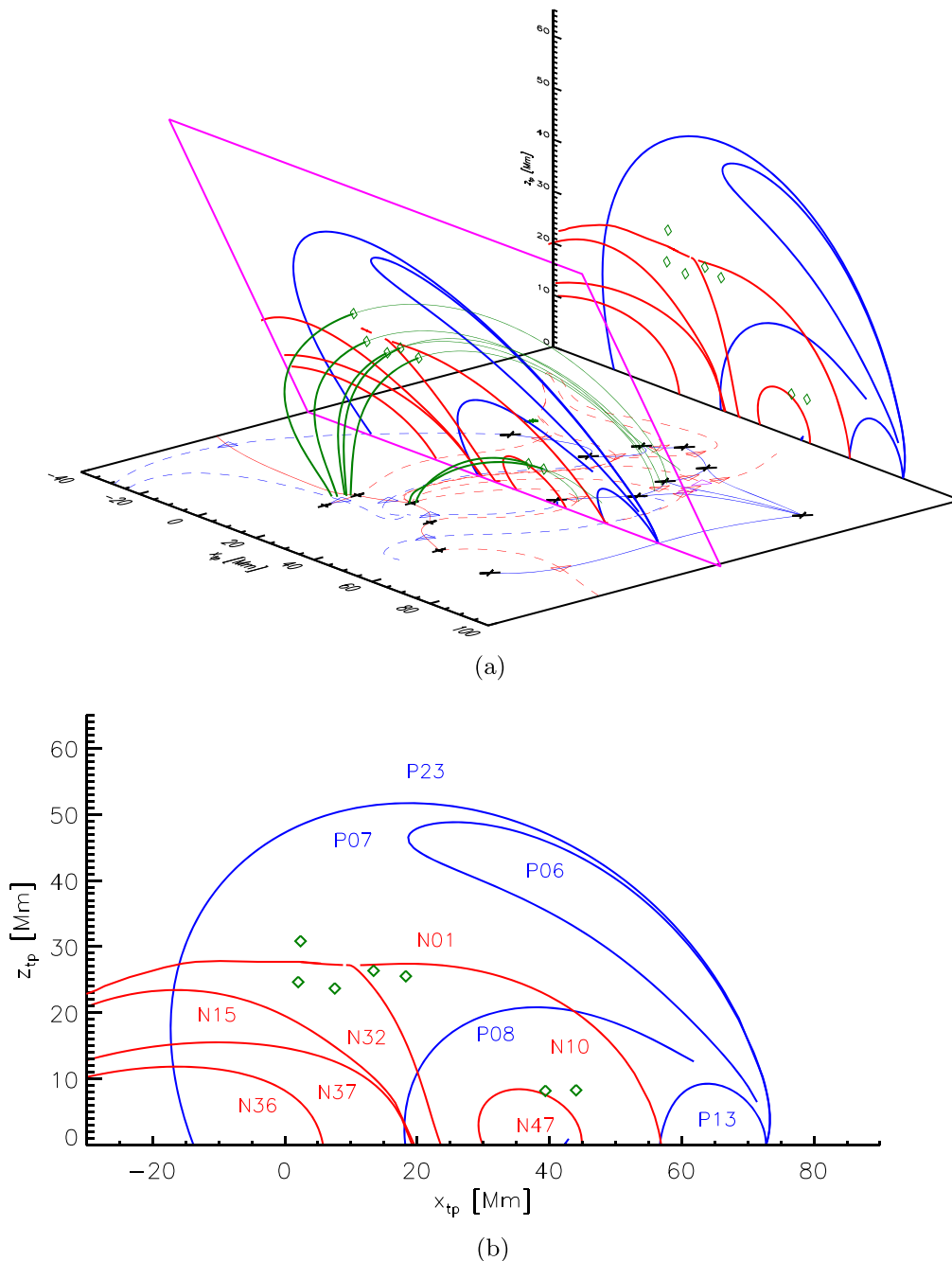
In the interest of consistency, we compute the QGR field using the same boundary data that had been used in Paper I to produce the LFFF models for α - h fitting. These fields provide the loops and α values informing the QGR field. That previous work, as well as the present work, uses a portion of the HMI LOS magnetogram rotated to appear as it would from directly above the point of tangency (originally at 42" E, 462" at 17:34). In the present case, this field is projected onto a 282×246 Mm rectangular region on the tangent plane. Following the methods of Paper I, the vertical component, B_z , is computed by assuming the observed LOS field is a component of a purely radial field. For computational convenience, the magnetogram is rotated onto a grid with 1.29×1.29 Mm pixels, reducing its native resolution. The gray scale of Figure 4(a) shows the central portion of the magnetogram after rotation and down-sampling, along with the horizontal axes of the computational volume, labeled in megameters (Mm). To mitigate effects of lateral boundaries, the projected magnetogram is surrounded on all four sides with 64.5 Mm (50 pixel) strips having $B_z = 0$. The entire 412×376 Mm rectangle forms the lower boundary, $z = 0$, of a rectilinear computational volume. The vertical grid has the same spacing as the horizontal, $\Delta z = 1.29$ Mm, and extends to $z = 246$ Mm. The full vector field, $\mathbf{B}(\mathbf{x})$ is represented on this $320 \times 292 \times 192$ point grid. Periodic boundary conditions are applied at the lateral boundaries and open conditions are applied at the top ($z = 246$ Mm) boundary.³

The QGR field fills the volume with a field that is approximately force free. This means that the Lorentz force,

$$\begin{aligned} \mathbf{J} \times \mathbf{B} &= \mathbf{B} \cdot \nabla \left(\frac{\mathbf{B}}{B} \right) - \frac{1}{2} \nabla_{\perp} B^2 \\ &= \mathbf{F}_{\text{mt}} + \mathbf{F}_{\text{mp}}, \end{aligned} \quad (1)$$

approximately vanishes at every grid point in the volume. In the various expressions above, $\mathbf{J} = \nabla \times \mathbf{B}$ is the current density, ∇_{\perp} is the gradient perpendicular to the magnetic field,

³ With additional constraint that field lines crossing lateral and top boundaries must carry no current.



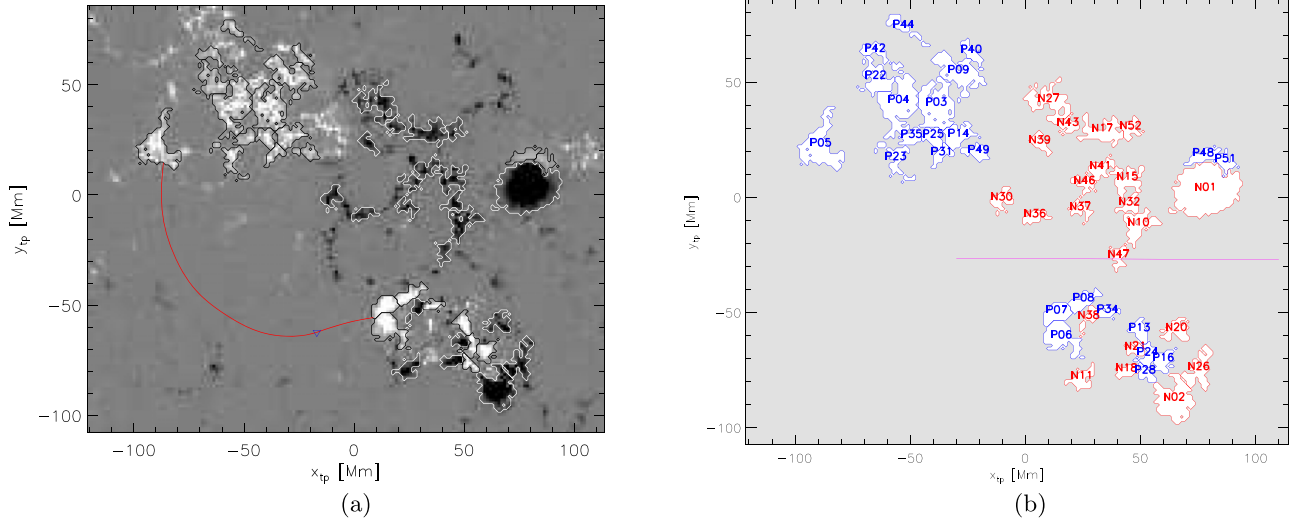


Figure 4. A central portion of the rotated and down-sampled HMI magnetogram used as the lower boundary condition of the QGR field, along with boundaries used to compare it to the MCT model: the regions used in defining the many-poles model. (a) Gray scale, saturated at ± 500 G shows the magnetogram. Black and white curves are the boundaries of the flux concentrations used to construct the MCT model. A blue triangle shows the null point in the QGR field, and red curves are the spines from that null point. The field of view from Figure 1(a) transformed by rotation to the view from above the point of tangency is outlined in magenta. (b) The labels for the flux concentrations. The gray region corresponds to weaker field which is disregarded by the MCT, but included in the QGR field. The horizontal magenta line shows the intersection of the dividing plane with the $z_{tp} = 0$ boundary.

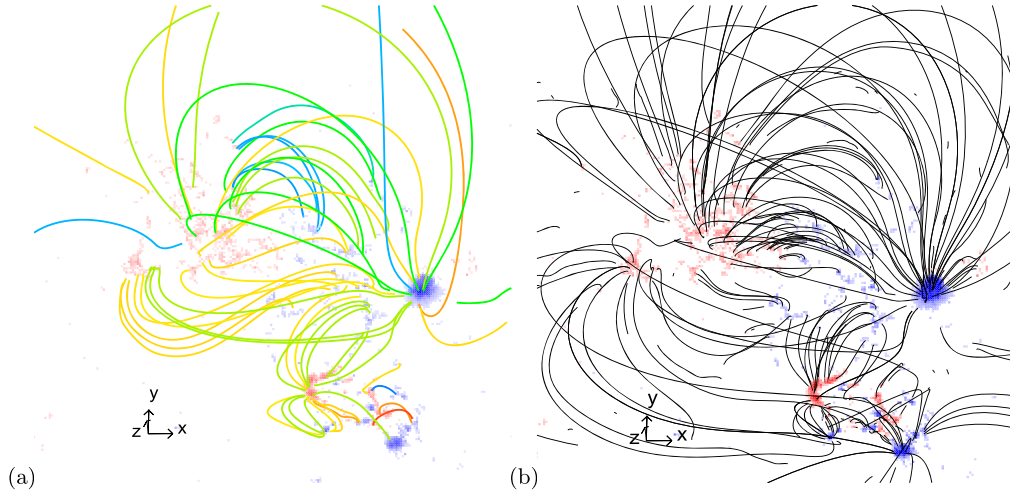


Figure 5. Perspective images of the QGR field viewed from along the LOS, with the LOS magnetogram in red/blue color scale along the $z = 0$ plane. (a) Loops in both ARs and the interconnecting domain fit using α - h fitting. Colors indicate the value of α for each loop, from $\alpha = -0.9 \times 10^{-2} \text{ Mm}^{-1}$ (blue) to $\alpha = +0.5 \times 10^{-2} \text{ Mm}^{-1}$ (yellow), and $\alpha = +2.9 \times 10^{-2} \text{ Mm}^{-1}$ (red), with green being around $\alpha = 0$. (b) 200 randomly selected field lines from the QGR field are plotted in black.

to characterize the degree to which F_{mt} and F_{mp} cancel one another while being less influenced by regions of low current. The QGR field is characterized by $\xi = 0.03$, corroborating its good approximation of a genuinely force-free field

The QGR method of Malanushenko et al. (2012) finds the force-free field, that best matches values of α along a sparse set of coronal field lines. We obtain these field lines, and their values of α , using the α - h fitting method described above (Malanushenko et al. 2009). In addition to the seven interconnecting loops already discussed, we perform α - h fits for 43 loops in AR 11147 and 29 in AR 11149. All 79 loops are shown in Figure 5(a) with colors representing the value of α inferred for that loop. This value is placed into the QGR fit along that line. Representative field lines from the final QGR field are shown in Figure 5(b).

The structure of the interconnecting flux in the QGR field is exhibited in the plots of $|\mathbf{B}(\mathbf{x})|$ and $\alpha(\mathbf{x})$ within the dividing plane shown in Figure 6. Interconnecting field lines lie beneath the blue solid curve. Figure 6(b) shows that $\alpha(\mathbf{x})$ does vary within the QGR field, albeit relatively smoothly over the interconnecting region.

3.1. Comparing the NLFFF to the Many-poles Model

While the QGR field is more realistic than the two MCT models, it shows structural similarity to each of them. Most significantly, the QGR field has a magnetic null point, shown in Figure 4(a), at a location similar to $B1$ in each of the MCT models. In MCT models the vertical field vanishes at $z = 0$ except at the point sources. As a result there is typically a family of null points, called *photospheric null points*, located

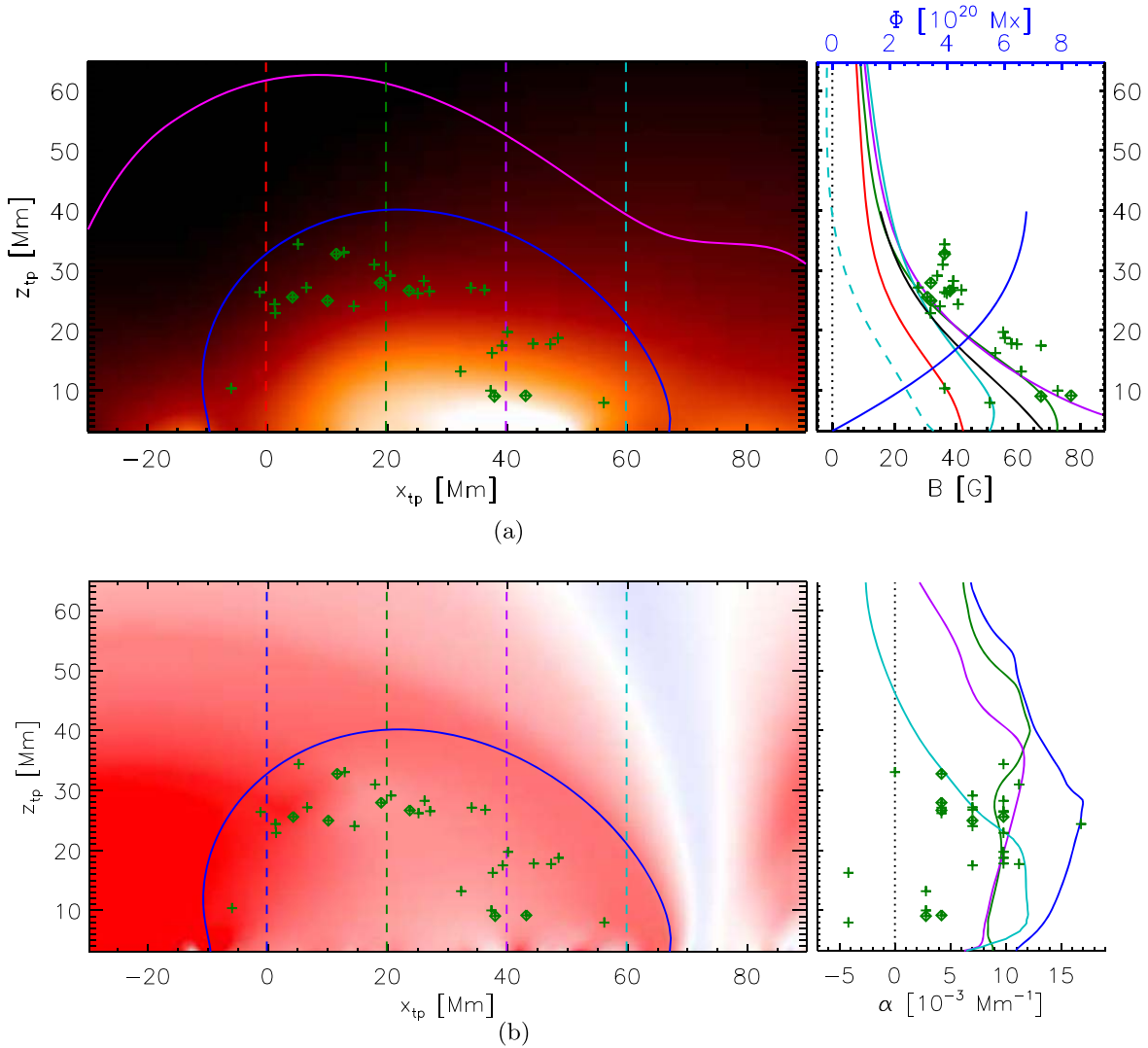


Figure 6. Magnetic field properties plotted on the back-projected dividing plane. A blue curve in each shows the separatrix from null point $B1$, beneath which lies all the interconnecting flux. (a) The local field strength at the dividing plane using a square-root-scaled color table saturated at 80 G. Values along four vertical slices (colored, vertical, dashed lines) are plotted against the right as a solid curve of the same colors. A black curve shows the mean value within the interconnecting flux. The component normal to the dividing plane, $B_n = \hat{n} \cdot \mathbf{B}$, along one slice is shown as a dashed curve of the same color. The curve $B_n = 0$ is shown as a magenta curve on the color scale. The locations where the 31 interconnecting loops (observed between 15:34 and 19:34) cross the dividing plane are shown as green pluses, and the seven visible at 17:34 (i.e., those from Figure 1(b)) as green diamonds. Field strengths of these loops are plotted with the same symbols on the right axis. The magnetic flux under the $B1$ separatrix (blue curve) crossing the dividing plane is integrated from $z = 0$ and plotted against the top axis on the right. (b) The value of α plotted in a format similar to (a), but on a scale from negative (blue) to positive (red) with white at $\alpha = 0$.

within the $z = 0$ plane (Longcope 2005). All the nulls shown by triangles in Figure 1(c) are photospheric null points. In contrast, the QGR model has a vertical magnetic field at $z = 0$ given by the magnetogram, so the magnetic field vector does not, in general, vanish within that plane. The null point of the QGR model is located at $z_{tp} = 7.1$ Mm, at the projected location shown in Figure 4(a). The null's two spine field lines (red curves in that figure) end in the $z = 0$ plane, one in AR 11147 and the other in AR 11149. As a result, the null's fan surface forms a genuine separatrix lying between volumes of flux originating from each AR. The QGR null therefore plays a topological role identical to null point $B1$ in each of the MCT models. The QGR does not, however, contain a null point analogous to $A2$, and thus does not include a genuine separator enclosing the interconnecting flux. The interconnecting flux in the QGR field can be identified, as in the MCT fields, using the intersection of the $B1$ separatrix with the dividing plane.

To make a more detailed comparison we use the QGR field to map the boundaries of the flux concentrations used in constructing the MCT field. These boundaries, shown in Figure 4(a), enclose significant regions with $|B_z(x, y, 0)| > 75$ G, and divide local maxima separated by sufficiently low saddle points (Barnes et al. 2005; Longcope et al. 2009). The region labels, shown in Figure 4(b), are those given to the point sources and shown in Figure 1(a) next to a region's flux-weighted centroid. The weak vertical field between the designated regions is given no label and appears light gray in Figure 4(b).

The region boundaries from Figure 4 are mapped along the QGR field lines to the dividing plane, then shown in Figure 7 in back-projection like Figure 3(b). The projected boundaries have structure similar to the separatrices in Figure 3(b). Boundaries between negative regions, shown in red, form concentric layers around the lower left, except for one small

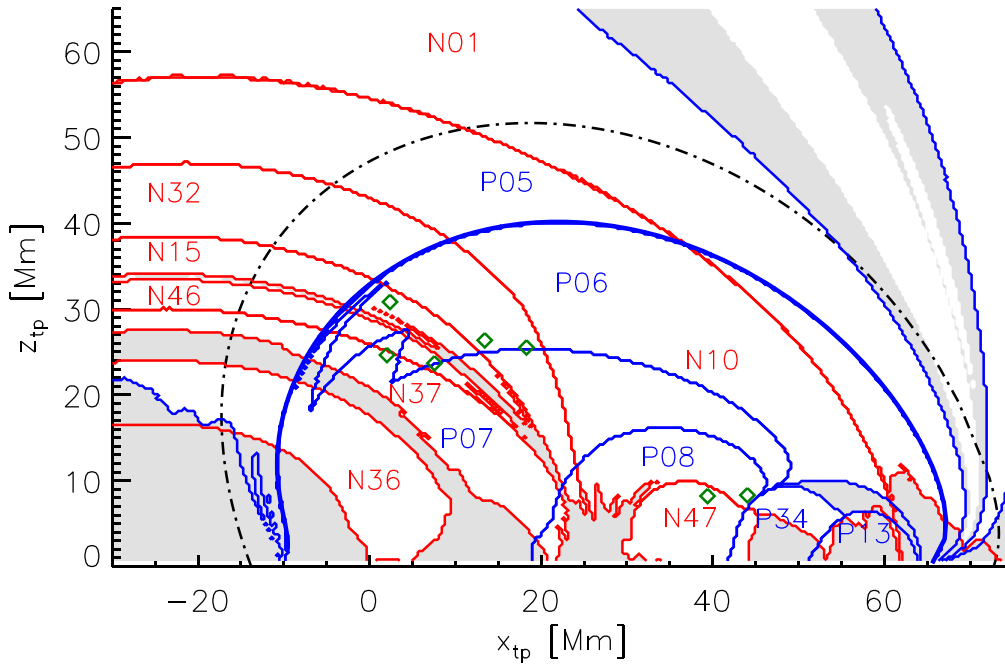


Figure 7. The region boundaries from Figure 4 mapped along the QGR field to the diving plane and shown in back-projection like Figure 3(b). Thin red and blue curves are from boundaries surrounding negative and positive regions, respectively. The thick blue curve is the fan surface from null point B1. Labeled white areas map to the region in the label. Light gray areas map to weak field outside the labeled regions. A black broken curve is the location of the fan surface from the many-poles MCT field. Green diamonds are the intersections of the seven coronal loops from Figures 1(b), 2, and 3.

N47 region surrounding the point $(x_{tp}, z_{tp}) = (40, 0)$ Mm. The ordering of the concentric regions is the same in the two although the N46 region is too thin to appear in Figure 3(b). Boundaries between positive regions, shown in blue, are also arranged in fashion similar to the separatrices in Figure 3(b). The MCT field does include a separatrix overlying P34 flux, but it proves to be numerically difficult to accurately trace, and is therefore not plotted.

The thicker blue curve on Figure 7 is the separatrix curve from the null point in the QGR field. This divides flux originating in the P05 region from that originating in either P06 or P07. These are the regions at the ends of the spines shown as red curves in Figure 4(a). The spines of B1 of the many-poles model connect to the nearby P23 source rather than to P05 itself.

Some of the interconnecting loops, shown once again by green diamonds, lie closer to the interconnecting separatrix (thick blue curve) in the QGR field than they had in either MCT model. This proximity is a result of a more accurate magnetic model, namely, the QGR, which is also more like the LFFs, extrapolated from the same magnetogram, used in α - h fitting. The fact that all field lines lie along a few of the projected region boundaries is therefore consistent with coronal loops energized by reconnection. Those very near the B1 separatrix may be loops recently reconnected to form interconnecting field. The lower loops, especially those around $z_{tp} = 10$ Mm, appear to have undergone internal reconnection. Those two lie near the intersection of the blue P08/P34 boundary and the red N10/N47 boundary. A similar intersection in the MCT model (which is not shown for the reasons given above) is a separator, but in the QGR field it is more likely to be a hyperbolic flux tube (Titov et al. 2003). This would be the site of internal reconnection whose energy release brightened those to coronal loops.

A more complete picture of the coronal loops is given by the frequency map, similar to Figure 13 of Paper I, showing 60 interconnecting coronal loops with starting times between 11:34 and 23:34 on 2011 January 21 (i.e., within 6 hr of 17:34), and successfully modeled by α - h fitting. Their three-dimensional field lines were rotated to 17:34 and their intersection with the dividing plane computed. A circle with diameter equal to the FWHM of the observed loop was placed with its center at the point of intersection. The color scale on Figure 8 shows the number of circles in which a point of the dividing plane is included. The regions in red have brightened six different times over the 12 hr interval, and the white areas never brightened at all.

The plot in Figure 8 corroborates the tendency for 171 Å loops to form near interior boundaries between photospheric flux concentrations. Those boundaries from Figure 7 are reproduced in black and violet over the color scale. Lines of loop concentration appear to follow the P06/P07 boundary higher up, and the P07/P08 boundary lower down. Equally important are several notable voids where very few loops appear. The largest of these, $-10 < x_{tp} < 20$ Mm and $z_{tp} < 20$ Mm, coincides with the middle of the P07 region, with no positive boundaries nearby. While voids in previous plots could be attributed to undersampling, these regions remain unbrightened over 12 hr, during which time other places have brightened up to six different times. A similar pattern was observed indirectly for large-scale structures and potential field extrapolations by Schrijver et al. (2010).

3.2. The QGR Field's Footpoint Mapping

The QGR's coronal field connects to the photosphere in a manner that retains some of the structure highlighted by the comparison to the MCT field. Figure 9 shows, in color, the field strength at the positive footpoint of each field line intersecting

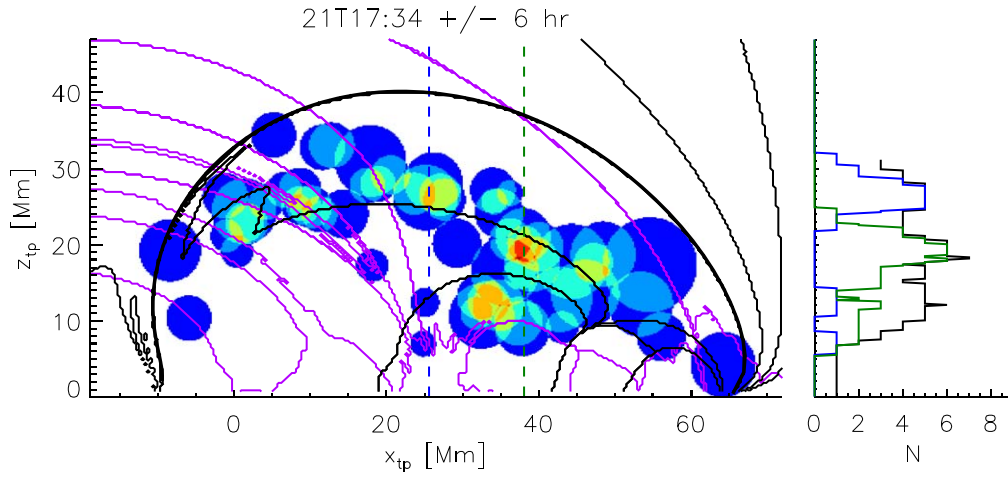


Figure 8. A map of brightening frequency over the 12 hr interval 11:34–23:34 on 2011 January 21, mapped on the back-projected dividing plane as described in the text. Colors from blue to red indicate the number of times a point is included in a different brightened loop. The curves along the right show, in green and blue, the counts along two vertical slices of the full map, whose locations are shown with dashed lines of the same color. Comparison shows that the peak color in the scale, red, corresponds to six loops including a single point. The black curve shows the maximum value at each height. Blue and red domain boundaries from Figure 7 are plotted in black and violet, respectively.

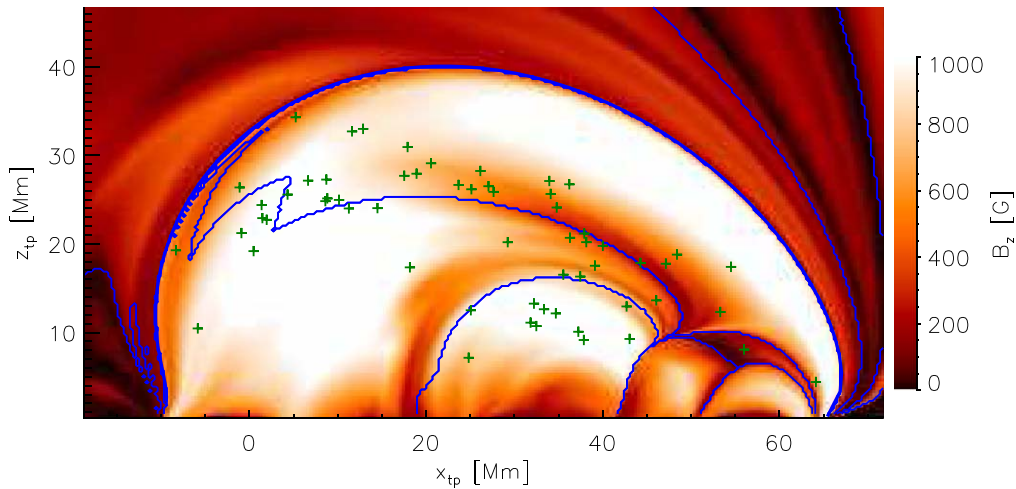


Figure 9. The field strength at the positive footpoint of each field line is plotted using a square-root color scale at the position it crosses the dividing plane. The color scale, plotted along the right, extends to much larger values than the local coronal field strengths plotted in Figure 6(a). Region boundaries are shown as thin blue curves, and the *B1* separatrix as a thick blue curve.

the dividing plane. The highly intermittent nature of the photospheric field gives the map of footpoint field strength far more structure than the local coronal field strength shown in Figure 6(a). Most notably, the region boundaries, shown as blue curves, appear to follow regions of weaker footpoint field strength. This is a natural consequence of the algorithm used to construct those boundaries (Barnes et al. 2005). Regions are grown “downhill” from local maxima in photospheric B_z , and boundaries pass through saddle points between pairs of maxima. This correspondence shows that the region boundaries used to replace separatrices, have their origin in the structure of the NLFFF.

The full field line mapping of the NLFFF contains more information than the topology heretofore described. The mapping describes how a positive footpoint, $\mathbf{X}^{(+)}$, is connected by its field line to a negative footpoint, $\mathbf{X}^{(-)}$. This connection is represented through a vector-valued function of vector argument $\mathbf{X}^{(-)}[\mathbf{X}^{(+)}$], or its inverse. A common method of characterizing this mapping function is through its derivative, which is a 2×2 Jacobian matrix (Longcope & Strauss 1994;

Titov et al. 2002; Pariat & Démoulin 2012; Liu et al. 2016). This matrix is related to the 3×3 matrix $M_{ij}(\ell)$ describing the linear mapping between three-dimensional neighborhoods of two points separated by a distance ℓ along the field line (Scott et al. 2017).

A field line satisfies the nonlinear ordinary differential equation

$$\frac{d\mathbf{x}}{d\ell} = \hat{\mathbf{b}}[\mathbf{x}(\ell)] = \frac{\mathbf{B}(\mathbf{x})}{|\mathbf{B}(\mathbf{x})|}, \quad (4)$$

where $\hat{\mathbf{b}}(\mathbf{x})$ is the unit vector tangent to the field line. If we designate a single field line $\mathbf{x}_0(\ell)$ as the central axis, then neighboring field lines are expressed as $\mathbf{x}(\ell) = \mathbf{x}_0(\ell) + \delta\mathbf{x}(\ell)$, where $\delta\mathbf{x}(\ell)$ is taken to be sufficiently small that all expansions can be terminated at linear order. Because of this linear assumption, the displacement from an arbitrary point, $\delta x_i(\ell)$, is proportional to its value at $\ell = 0$ through a 3×3 neighborhood-mapping matrix, $\delta x_i(\ell) = M_{ij}(\ell)\delta x_j(0)$, where repeated indices are summed from 1–3. Substituting this into Equation (4) and

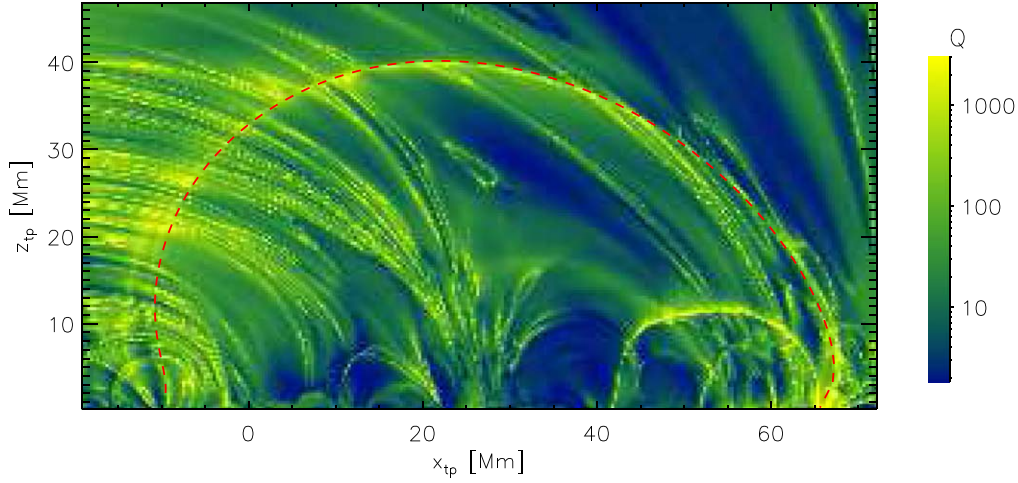


Figure 10. The end-to-end squashing factor Q , defined by Equation (8), plotted in back-projection on the dividing plane using a logarithmic color table, shown along the right. A red-dashed curve shows the genuine separatrix formed by the fan surface from null point B1.

keeping only linear terms yields the equation governing the neighborhood mapping

$$\frac{dM_{ij}}{d\ell} = \frac{1}{|\mathbf{B}|} (\delta_{ik} - \hat{b}_i \hat{b}_k) \frac{\partial B_k}{\partial x_n} M_{nj}. \quad (5)$$

The matrix $M_{ij}(\ell)$ is computed by using Equation (4) to trace a central field line from a point on the dividing plane ($\ell = 0$) and solving Equation (5) at the same time, initialized with the identity: $M_{ij}(0) = \delta_{ij}$. The field line is first followed in the direction of $\hat{\mathbf{b}}$ (i.e., ℓ increasing from $\ell = 0$) until it ends at a point of negative photospheric flux ($B_z < 0$) after a distance $\ell_- > 0$. The matrix at that point is denoted $M_{ij}^{(-)} = M_{ij}(\ell_-)$. Following the central field line in the opposite direction (i.e., ℓ decreasing from zero) ends at a point of positive photospheric flux at $\ell_+ < 0$, where the matrix is $M_{ij}^{(+)} = M_{ij}(\ell_+)$. Each point on the dividing plane will therefore have two 3×3 matrices, $M_{ij}^{(-)}$ and $M_{ij}^{(+)}$, describing how its local neighborhood maps to the neighborhoods of its two footpoints.

The mapping between three-dimensional neighborhoods, given by the 3×3 matrix $M_{ij}^{(\pm)}$, can be restricted to a mapping between two-dimensional planes. Points on the dividing plane are designated using two coordinates ξ_1 and ξ_2 , while points on one of the photospheric surfaces are written with coordinates $X_1^{(\pm)}$ and $X_2^{(\pm)}$. The mapping between these two planes is a 2×2 matrix

$$\frac{\partial X_a^{(\pm)}}{\partial \xi_b} = \tilde{M}_{ab}^{(\pm)} = \hat{\mathbf{X}}_a \cdot \left(\mathbf{I} - \frac{\mathbf{B}^{(\pm)} \hat{\mathbf{z}}}{B_z^{(\pm)}} \right) \cdot \mathbf{M}^{(\pm)} \cdot \hat{\xi}_b, \quad (6)$$

where a and b each take on values 1 and 2 independently, $\mathbf{B}^{(\pm)}$ is the magnetic field vector at the footpoint, $\hat{\mathbf{z}}$ is the vertical, normal to the photosphere, and \mathbf{I} is the 3×3 identity matrix. The matrix in parentheses projects along the field line to the photospheric plane (Titov 2007). One pair of orthogonal unit vectors, $\hat{\mathbf{X}}_1$ and $\hat{\mathbf{X}}_2$, lie in the photospheric plane, while another pair, $\hat{\xi}_1$ and $\hat{\xi}_2$, lie in the dividing plane. A field line that crosses the dividing plane at a point separated from the central field line by $\delta \xi = \delta \xi_b \hat{\xi}_b$ will cross one photospheric plane $\delta \mathbf{X}^{(\pm)} = \delta X_a^{(\pm)} \hat{\mathbf{X}}_a$ from the central footpoint, where $\delta X_a^{(\pm)} = \tilde{M}_{ab}^{(\pm)} \delta \xi_b$. (Repeated index b is summed from 1–2.)

The end-to-end mapping from one photospheric footpoint to the other is characterized by the composite mapping generated by the matrix product

$$D_{ab} = [\tilde{\mathbf{M}}^{(-)}]_{ac} [(\tilde{\mathbf{M}}^{(+)})^{-1}]_{cb} = \frac{\partial X_a^{(-)}}{\partial X_b^{(+)}}. \quad (7)$$

This matrix is the derivative of the photosphere-to-photosphere footpoint mapping mentioned above. A common way to characterize it is through the so-called *squashing factor* (Titov et al. 2002; Pariat & Démoulin 2012)

$$Q = \frac{\text{Tr}(\mathbf{D}^T \cdot \mathbf{D})}{|\det(\mathbf{D})|} = \frac{D_{ab} D_{ab}}{|D_{11} D_{22} - D_{12} D_{21}|}. \quad (8)$$

The inverse mapping, from $\mathbf{X}^{(-)} \rightarrow \mathbf{X}^{(+)}$, will have a derivative matrix given by the inverse of the forward mapping $\partial \mathbf{X}^{(+)} / \partial \mathbf{X}^{(-)} = [\partial \mathbf{X}^{(-)} / \partial \mathbf{X}^{(+)}]^{-1}$. It can be shown that computing Q with the inverse matrix yields the same value, so the squashing factor is a property of the field line.

The squashing factor, computed in this manner for field lines traced forward and backward from the dividing plane, is plotted on the projected dividing plane in Figure 10. Regions where Q is finite but large are known as QSLs (Priest & Démoulin 1995; Titov et al. 2002). Several yellow bands appear to fit this description, although with values of $Q \simeq 1000$ they are weaker than many QSLs reported in the literature (Savcheva et al. 2015; Chintzoglou et al. 2017; Masson et al. 2017). There is a layer of modest squashing ($Q \simeq 500$) around the separatrix from null point B1. This is a *genuine* separatrix at which the end-to-end mapping, $\mathbf{X}^{(-)}[\mathbf{X}^{(+)}$, is discontinuous. The derivative matrix, D_{ab} , will diverge at the discontinuity in the manner of a Dirac- δ function: it will be infinite, but only on a layer of zero thickness.⁴ Because it occupies zero area, points selected on the dividing plane never fall on it, and the squashing factor

⁴ Many investigators compute the end-to-end derivative matrix from Equation (7), using a finite difference approximation from a gridded representation of the mapping function, $X_a^{(-)}[X_1^{(+)}, X_2^{(+)}]$. In a finite difference approximation, the mapping discontinuity created by a *genuine* separatrix will have a large but finite value. The value is inversely proportional to the grid spacing, so it will become ever larger under refinement of the grid. Since they appear in such finite difference computations with large values of Q , genuine separatrices are sometimes included under the term QSL—“quasi”-separatrix layers. Our direct computation of M_{ab} shows only genuine QSLs, so separatrices must be identified through other means.

is never computed for any point on the separatrix. The region around the separatrix is somewhat deformed, endowing it with the modest value of Q shown in Figure 10. Several of the QSLs have counterparts in the map of region boundaries on Figure 7, which are in turn related to separatrices in the many-poles MCT model.

3.3. Characterizing Noncircular Loop Cross Sections

Malanushenko et al. (2014) argued that variation in a loop's cross section, along its axis, might play a significant role in the visibility of EUV loops. If the coronal portion of a loop had a highly oblate cross section then it would stand out against the background most when viewed edge-on. The one-sided mapping matrices $\tilde{M}_{ab}^{(\pm)}$ describe the variation in cross section and can thus be used to test this hypothesis in the current data set.

We begin by assuming the loop is selected and energized by an approximately isotropic process near one of its footpoints. Under this assumption the full loop would consist of the bundle of field lines anchored within some small distance δr of that footpoint: $|\delta \mathbf{X}^{(\pm)}|^2 < \delta r^2$. This circular footpoint region will map to a set of points on the dividing plane $\delta \xi$ from the central field line's crossing, where

$$\begin{aligned} |\delta \mathbf{X}^{(\pm)}|^2 &= \tilde{M}_{ca}^{(\pm)} \tilde{M}_{cb}^{(\pm)} \delta \xi_a \delta \xi_b \\ &= \tilde{S}_{ab}^{(\pm)} \delta \xi_a \delta \xi_b < \delta r^2. \end{aligned} \quad (9)$$

This is an ellipse defined by the 2×2 symmetric matrix $\tilde{S}_{ab}^{(\pm)} = \tilde{M}_{ca}^{(\pm)} \tilde{M}_{cb}^{(\pm)}$, whose superscript designates which footpoint was isotropically energized to create the loop.

The elliptic cross section within the dividing plane is characterized by the ratio of its major to minor axes, R_{\pm} . This is equal to the square root of the ratio of largest to smallest eigenvalues of the symmetric matrix $\tilde{S}_{ab}^{(\pm)}$. It is also related to the one-sided squashing factor

$$Q^{(\pm)} = \frac{\text{Tr}(\tilde{S}^{(\pm)})}{\sqrt{\det(\tilde{S}^{(\pm)})}} = R_{\pm} + R_{\pm}^{-1}. \quad (10)$$

Figure 11 shows $Q^{(+)}$ and $Q^{(-)}$ over the projected dividing plane. Several of the QSLs visible in the full squashing factor, Q plotted in Figure 10, have counterparts in $Q^{(+)}$. These are field lines whose neighborhood undergoes most deformation on the positive side of the dividing plane. They are the QSLs corresponding to positive (blue) region boundaries on Figure 7. The B1 null point is on the positive side so its separatrix appears inside a modest lane of enhancement in $Q^{(+)}$. Other QSLs are visible in Q , which are absent from $Q^{(+)}$, but do appear in $Q^{(-)}$ (Figure 11(b)). These correspond most closely with the negative (red) region boundaries on Figure 7.

The long axis of the elliptic cross section is along the eigenvector of $\tilde{S}^{(\pm)}$ with the smallest eigenvalue. Figure 12 shows several of these ellipses in the dividing plane where they would appear as loop cross sections. Many of the ellipses in Figure 12(a), and some in Figure 12(b), have small eccentricities,⁵ $Q^{(\pm)} < 4$; the medians are $\text{med}[Q^{(+)}] = 4.0$ and $\text{med}[Q^{(-)}] = 7.0$. Each ellipse is scaled to make its apparent width, viewed along the LOS, match the full width measured in the AIA 171 Å image.

The area of the rescaled ellipse will differ from the circular cross section with the same apparent diameter. We denote by r_A the ratio of elliptical to circular areas for a given loop. Ellipses whose major axis makes a significant angle with respect to the LOS will have small values, $r_A \sim 2/Q^{(\pm)}$. Those nearly aligned will have large values $r_A \sim Q^{(\pm)}$. Aligned ellipses with very large r_A are rare (only four have $r_A > 1$) although a few cases on Figure 12(b) would have appeared too large to plot, and have been reduced for plotting purposes.

Values of the area ratio r_A are generally small, meaning that on the whole the ellipses have smaller areas than their corresponding circles would have. Median values are $\text{med}(r_A) = 0.34$ for Figure 12(a) and $\text{med}(r_A) = 0.21$ for Figure 12(b). One consequence of this is that the total flux from the collection of elliptic loops would be correspondingly smaller, probably bringing it into line with the total interconnecting flux. Nevertheless, the ellipses appear to overlap, albeit less than the circles did (i.e., Figure 8), suggesting that even under the hypothesis of elliptical cross sections, some flux would need to be energized multiple times.

As pointed out by Malanushenko et al. (2014), the ratio of elliptic to circular areas would affect the apparent brightness of a loop. It would therefore affect the plasma density inferred from the loop's observed emission measure. It is common practice to assume circular cross sections and thus equate the LOS through the loop to its apparent diameter (Kano & Tsuneta 1995; Aschwanden et al. 2000). Investigators following the practice have reported that loops such as ours, with $T \sim 10^6$ K, have plasma densities larger than that of a loop in mechanical equilibrium (Winebarger et al. 2003; Klimchuk 2006). This is true for our loops as well, with the ratio of observed to equilibrium density being 3.7. It turns out, however, that using the density from the circular assumption yields a radiative cooling time consistent, on average, with the observed lifetime of the loop (see Paper I). The average LOS through a rescaled ellipse will be a factor r_A times that of the equivalent circle, making the inferred plasma density larger by a factor $r_A^{-1/2}$. This decreases the radiative cooling times by $r_A^{1/2}$, bringing them to a value, on average, half the loop's lifetime. This makes it seem less likely that the loop cross sections are in fact elliptical at the dividing plane.

It is also notable that the loops actually observed are not preferentially aligned along the LOS. To appreciate this compare the long axes of the ellipses in Figure 12 with the arrow showing the LOS. The hypothesis of elliptical cross sections does not, therefore, help explain why we observe the loops we actually do observe.

The foregoing discussion worked from the hypothesis that loops were defined and energized by an isotropic process at one footpoint. This would create a circular cross section at one footpoint that mapped to the ellipses plotted in Figure 12. The alternative would be for loops to be defined and energized by an isotropic process in the corona, perhaps magnetic reconnection by isotropically enhanced resistivity. Under this hypothesis the loops would have circular cross sections near their apices, which map to elliptical cross sections near their feet. These ellipses would have the same aspect ratio as those plotted in Figure 12, although with differing sizes and orientations. Comparing cross sections of a given loop (i.e., between Figures 12(a) and (b)) shows that one footpoint would generally be more eccentric than the other. This is consistent with our previous observation that values of $Q^{(+)}$ and $Q^{(-)}$ arise

⁵ Similar results were found by Malanushenko et al. (2014) for potential fields they investigated.

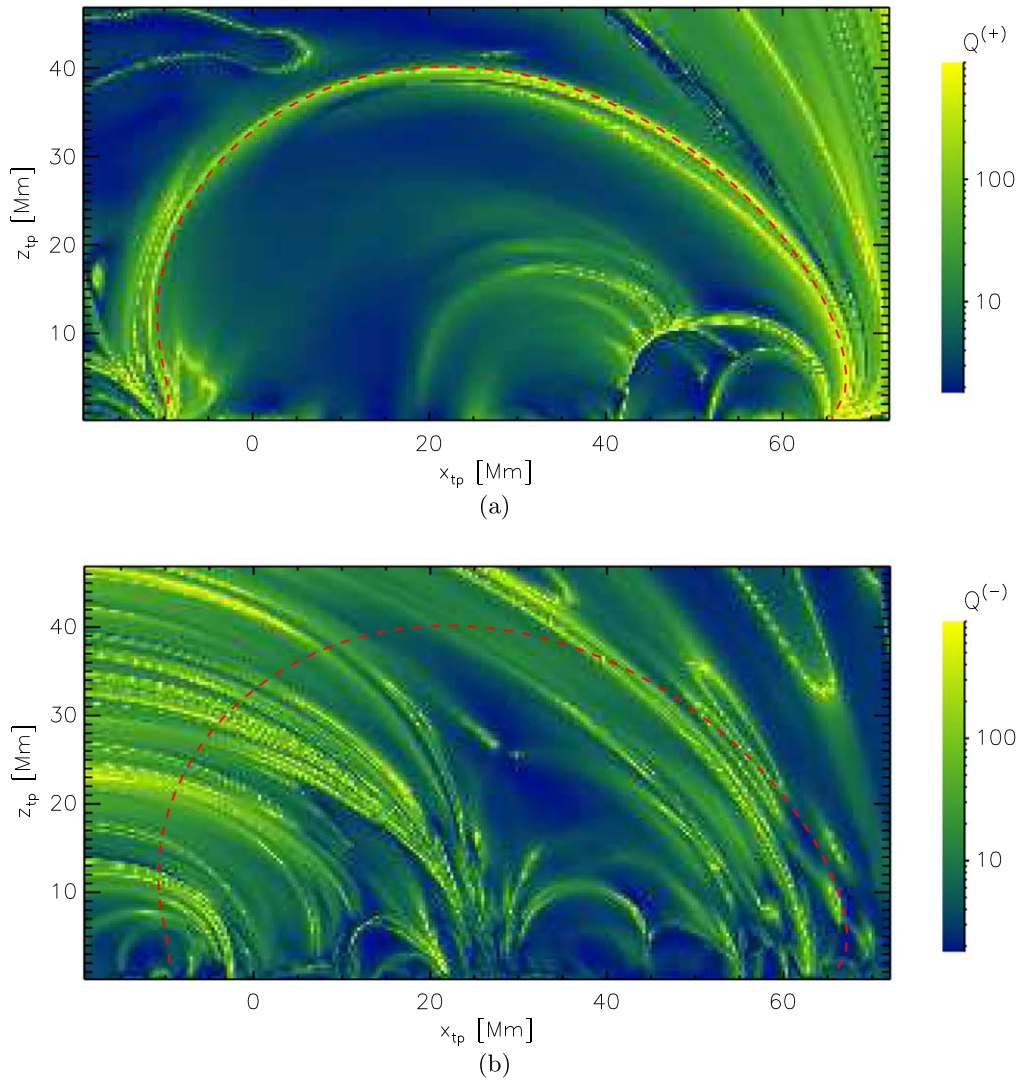


Figure 11. Plots of the one-sided squashing factors (a) $Q^{(+)}$ and (b) $Q^{(-)}$ defined in Equation (10), plotted in back-projection on the dividing plane using a logarithmic color table, shown along the right. A red-dashed curve shows the genuine separatrix formed by the fan surface from null point B1.

from distortions near that one end. In light of the above discussion of visibility, we expect that one of the two footpoints of a loop might be less visible. Indeed, we had noted this tendency when tracing loops in the 171 Å images.

4. Discussion

The set of interconnecting loops identified and characterized by Paper I provide evidence that the volume of magnetic field between the ARs continues to be heated well after its initial reconnection. The modeling presented above suggests that the bright loops tend to form along internal magnetic boundaries in the interconnecting domain, such as separatrices. It was argued in the introduction of this work that the hypothesis of magnetic reconnection selecting and energizing coronal loops predicts the kind of nonuniform structuring that we ultimately find: loops concentrated along separatrices.

We have interpreted the loop locations using three different magnetic field models. The least sophisticated, the quadrupolar MCT model used in Paper I, is able to characterize reconnection creating interconnecting field from field lines of each region; we refer to this as external reconnection. To characterize reconnection *internal* to the interconnecting

domain we turn to the many-poles MCT model, described in Section 2.1, and the NLFFF model obtained through the QGR method described in Section 3. The MCT model has a set of separatrices, but suffers from being a linear force-free field. We found the QGR field to have many features in common with the MCT field. It has a single genuine separatrix overlying the interconnecting domain, similar to that of the MCT. In place of internal separatrices it has QSLs, which tend to follow the separatrices of the MCT field. The bright loops identified in Paper I seem to occur along similar lines and seem to avoid the regions interior to magnetic domains.

All of these are equilibrium models are of a single time, 17:34 2011 January 21, which we deemed to be representative of the period of emergence and continued heating. In order to obtain a detailed map of the coronal loop distribution we used loops from first a 4 hr and then a 12 hr interval centered on that time. While the coronal magnetic field undoubtedly evolves during these intervals, we do not expect it to change enough to negate our conclusions. As the photospheric field evolves, and as reconnection proceeds, the separatrices will definitely move and field lines will move relative to them. Both of these motions will, however, be slow enough that we do not expect a sizable

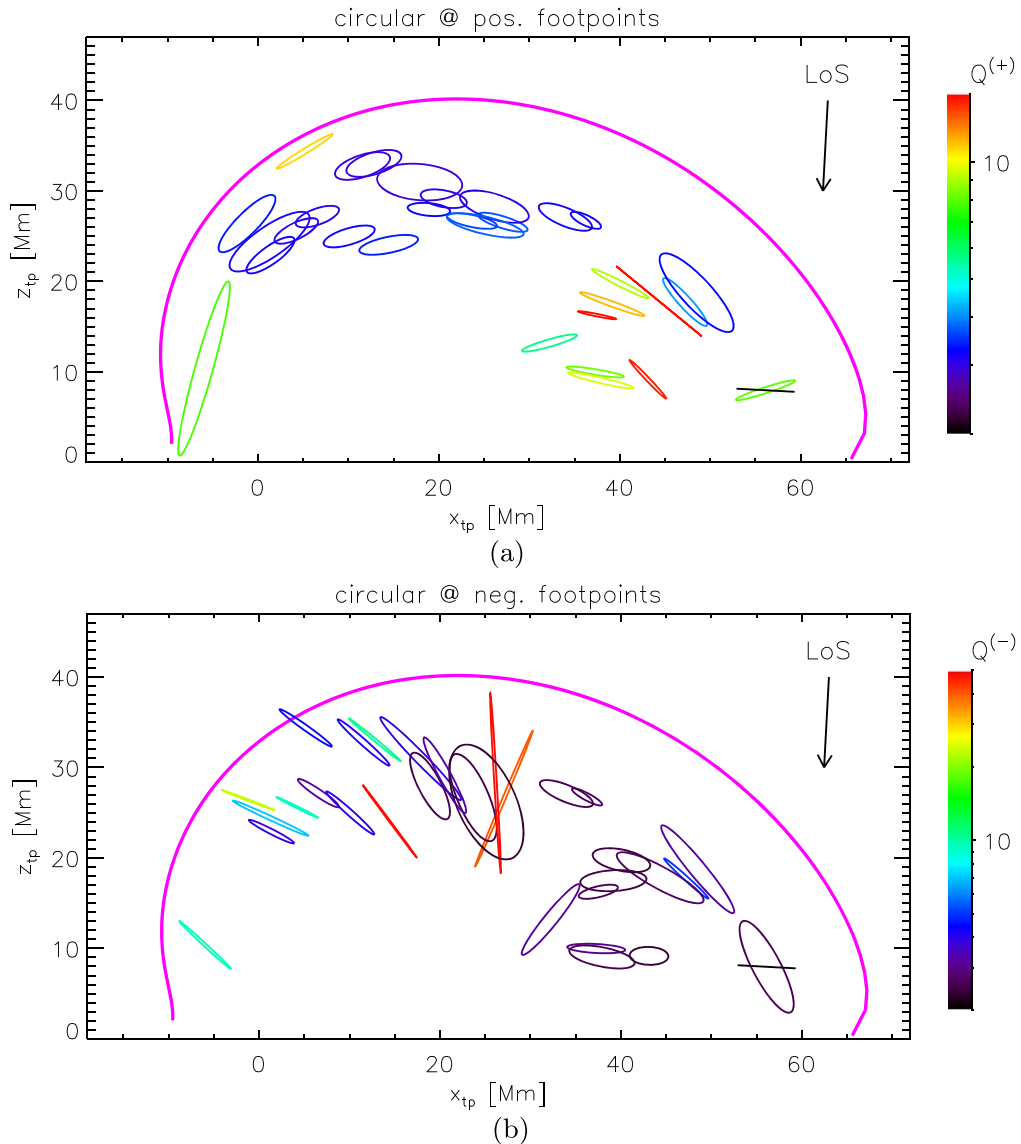


Figure 12. Loop cross sections under the assumption of isotropic energization from (a) the positive footpoint and (b) the negative footpoint. Ellipses are scaled so the apparent width matches the full width in the 171 Å image. The full width is shown as a black line segment through the right-most loop. This is done for the same 31 loops appearing within 2 hr of 17:34 also shown in Figure 6. The direction of the line of sight is shown as an arrow. The magenta curve shows the genuine separatrix formed by the fan surface from null point B1. The color of each ellipse corresponds to its one-sided squashing factor indicated by a color bar on the right.

separation during the approximately hour-long life of a loop. The small displacement may slightly broaden the apparent layers (evident in Figure 8) but probably cannot fill in the voids.

The boundaries in the two sophisticated magnetic models are complex. The many-poles MCT model includes three positive and seven negative internal separatrices shown in Figure 7(b). The map of the squashing factor, Figure 10, shows numerous linear features suggestive of QSLs. These details are absent from the frequency map generated from 60 loops identified over a 12 hr interval, shown in Figure 8. We can think of several explanations for this discrepancy. A density plot made from only 60 points will necessarily be coarse and lack fine detail. The magnetic evolution described above will further blur details. Finally, models invoke separatrices and/or QSLs as necessary but not sufficient for current sheet formation and reconnection. There may be other factors determining which boundaries are undergoing reconnection, which loops are energized, or which energized loops are most visible. For these reasons we do find

support in the loop concentrations for the reconnection hypothesis, in spite of the lack of detailed correspondence.

The degree of agreement shown between the separatrices in the MCT model and the QSLs in the QGR model is worthy of note. Studies of reconnection typically use one of these approaches but rarely both. The two have been related in idealized cases such as theoretical quadrupoles with a single separator (Démoulin et al. 1996; Titov & Hornig 2002). Our work shows how they are related in observed field configurations of much greater complexity. Neither of our models is a potential field, nor does either contain anything like a current sheet. In each case, therefore, the boundary reflects a place where current would be prone to form.

The cross section of a given flux bundle will naturally vary along its length. If the bundle was defined and given a circular cross section at one footpoint, its cross section would be elliptical high in the corona. In this case the common practice of assuming a circular cross section would underestimate the

loop's plasma density and thus overestimate its radiative lifetime. We find, however, that the radiative lifetimes computed under the assumption of a circular cross section agree with the observed lifetimes. The corollary is that assuming elliptic cross sections in the corona would create a disagreement with observations. We therefore find it more likely that the bundles have circular cross section in the corona. This could be a result of being formed by reconnection there. If the loops followed the form of the large-scale field, such as our NLFFF, their cross section would become elliptical near one footpoint, making it potentially more difficult to observe there. This is consistent with the general tendency for coronal loops, including those in our study, to be clearly visible over some portion, not generally extending to both feet.

Some studies have noted, however, that the apparent diameter of a loop does not vary along its length as one would expect if its cross section were anywhere noncircular (Klimchuk et al. 1992). This may be a consequence of twist within the loop possibly injected by the very reconnection process that created it (Wright & Berger 1989). In that case the magnetic structure within the loop would differ from that of the surrounding field, making any large-scale model, including the NLFFF, less useful in understanding its properties. It therefore remains a possibility that the cross sections of observed coronal loops, including those in our study, are not well characterized by global quantities such as the squashing factor.

Our analysis is based entirely on loops observed in a single band of AIA—171 Å. It is possible that loops found this way differ in some systematic way from the surrounding magnetic flux. We have worked under the assumption that once a loop is impulsively heated it cools until it becomes visible in 171 Å images. Our lifetime measurements show that loops appearing in 171 Å are consistent with free cooling, suggesting that our sample does reflect the set of flux that has been impulsively energized. There may be other flux energized in some other way that does not appear as a loop in this cool band. There could even be a population of impulsively heated loops that do not cool to low enough temperature to appear in 171 Å. Such loops, if they exist, will need to be sought and characterized through other means.

This work was supported by NASA's HGI program under grant NNX16AF81G. The authors thank the anonymous referee for comments that helped improve the manuscript. Computational efforts were performed on the Hyalite High Performance Computing System, operated and supported by University Information Technology Research Cyberinfrastructure at Montana State University.

ORCID iDs

Marika McCarthy  <https://orcid.org/0000-0002-5951-0000>

References

- Aschwanden, M. J., & Alexander, D. 2001, *SoPh*, **204**, 91
- Aschwanden, M. J., Nightingale, R. W., & Alexander, D. 2000, *ApJ*, **541**, 1059
- Aulanier, G., Parlat, É., & Démoulin, P. 2005, *A&A*, **444**, 961
- Bagalá, L. G., Mandrini, C. H., Rovira, M. G., Démoulin, P., & Hénoux, C. H. 1995, *SoPh*, **161**, 103
- Barnes, G., Longcope, D. W., & Leka, K. D. 2005, *ApJ*, **629**, 561
- Baum, P. J., & Bratenahl, A. 1980, *SoPh*, **67**, 245
- Beveridge, C., Longcope, D. W., & Priest, E. R. 2003, *SoPh*, **216**, 27
- Chintzoglou, G., Vourlidas, A., Savcheva, A., et al. 2017, *ApJ*, **843**, 93
- Chiu, Y. T., & Hilton, H. H. 1977, *ApJ*, **212**, 873
- Close, R. M., Parnell, C. E., Longcope, D. W., & Priest, E. R. 2004, *ApJL*, **612**, L81
- De Rosa, M. L., Schrijver, C. J., Barnes, G., et al. 2009, *ApJ*, **696**, 1780
- Démoulin, P., Hénoux, J. C., Priest, E. R., & Mandrini, C. 1996, *A&A*, **308**, 643
- Démoulin, P., van Driel-Gesztelyi, L., Schmieder, B., et al. 1993, *A&A*, **271**, 292
- Galeev, A. A., Rosner, R., Serio, S., & Vaiana, G. S. 1981, *ApJ*, **243**, 301
- Galsgaard, K., Priest, E. R., & Nordlund, Å. 2000, *SoPh*, **193**, 1
- Greene, J. M. 1988, *JGR*, **93**, 8583
- Hénoux, J. C., & Somov, B. V. 1987, *A&A*, **185**, 306
- Heyvaerts, J., & Priest, E. R. 1984, *A&A*, **137**, 63
- Kano, R., & Tsuneta, S. 1995, *ApJ*, **454**, 934
- Klimchuk, J., Lemen, J., Feldman, U., Tsuneta, S., & Uchida, Y. 1992, *PASJ*, **44**, L181
- Klimchuk, J. A. 2006, *SoPh*, **234**, 41
- Lau, Y.-T., & Finn, J. M. 1990, *ApJ*, **350**, 672
- Lemen, J. R., Title, A. M., Akin, D. J., et al. 2012, *SoPh*, **275**, 17
- Litwin, C., & Rosner, R. 1993, *ApJ*, **412**, 375
- Liu, R., Kliem, B., Titov, V. S., et al. 2016, *ApJ*, **818**, 148
- Longcope, D., Unverferth, J., Klein, C., McCarthy, M., & Priest, E. 2018, *ApJ*, **868**, 148
- Longcope, D. W. 1996, *SoPh*, **169**, 91
- Longcope, D. W. 2005, *LRSF*, **2**, 7
- Longcope, D. W., Barnes, G., & Beveridge, C. 2009, *ApJ*, **693**, 97
- Longcope, D. W., Des Jardins, A. C., Carranza-Fulmer, T., & Qiu, J. 2010, *SoPh*, **267**, 107
- Longcope, D. W., Kankelborg, C. C., Nelson, J. L., & Pevtsov, A. A. 2001, *ApJ*, **553**, 429
- Longcope, D. W., & Klapper, I. 2002, *ApJ*, **579**, 468
- Longcope, D. W., McKenzie, D., Cirtain, J., & Scott, J. 2005, *ApJ*, **630**, 596
- Longcope, D. W., & Silva, A. V. R. 1998, *SoPh*, **179**, 349
- Longcope, D. W., & Strauss, H. R. 1994, *ApJ*, **426**, 742
- Malanushenko, A., Longcope, D. W., Fan, Y., & Gibson, S. E. 2009, *ApJ*, **702**, 580
- Malanushenko, A., Longcope, D. W., & McKenzie, D. E. 2009, *ApJ*, **707**, 1044
- Malanushenko, A., Schrijver, C. J., DeRosa, M. L., & Wheatland, M. S. 2014, *ApJ*, **783**, 102
- Malanushenko, A., Schrijver, C. J., DeRosa, M. L., Wheatland, M. S., & Gilchrist, S. A. 2012, *ApJ*, **756**, 153
- Mandrini, C. H., Démoulin, P., Hénoux, J. C., & Machado, M. E. 1991, *A&A*, **250**, 541
- Masson, S., Parlat, É., Valori, G., et al. 2017, *A&A*, **604**, A76
- McCarthy, M. I., Longcope, D. W., Malanushenko, A., & McKenzie, D. E. 2019, *ApJ*, **887**, 140
- McKenzie, D. E., & Savage, S. L. 2011, *ApJL*, **735**, L6
- Metcalf, T. R., De Rosa, M. L., Schrijver, C. J., et al. 2008, *SoPh*, **247**, 269
- Nandy, D., Hahn, M., Canfield, R. C., & Longcope, D. W. 2003, *ApJL*, **597**, L73
- Pariat, É., & Démoulin, P. 2012, *A&A*, **541**, A78
- Parker, E. N. 1983, *ApJ*, **264**, 635
- Priest, E. R., Bungey, T. N., & Titov, V. S. 1997, *GApFD*, **84**, 127
- Priest, E. R., & Démoulin, P. 1995, *JGR*, **100**, 23,443
- Priest, E. R., Heyvaerts, J. F., & Title, A. M. 2002, *ApJ*, **576**, 533
- Priest, E. R., Longcope, D. W., & Heyvaerts, J. 2005, *ApJ*, **624**, 1057
- Qiu, J., & Longcope, D. W. 2016, *ApJ*, **820**, 14
- Rosner, R., Tucker, W. H., & Vaiana, G. S. 1978, *ApJ*, **220**, 643
- Savcheva, A., Parlat, É., McKillop, S., et al. 2015, *ApJ*, **810**, 96
- Scherrer, P. H., Schou, J., Bush, R. I., et al. 2012, *SoPh*, **275**, 207
- Schrijver, C. J., DeRosa, M. L., & Title, A. M. 2010, *ApJ*, **719**, 1083
- Scott, R. B., Pontin, D. I., & Hornig, G. 2017, *ApJ*, **848**, 117
- Tarr, L. A., Longcope, D. W., McKenzie, D. E., & Yoshimura, K. 2014, *SoPh*, **289**, 3331
- Taylor, J. B. 1974, *PhRvL*, **33**, 1139
- Titov, V. S. 2007, *ApJ*, **660**, 863
- Titov, V. S., Galsgaard, K., & Neukirch, T. 2003, *ApJ*, **582**, 1172
- Titov, V. S., & Hornig, G. 2002, *AdSpR*, **29**, 1087
- Titov, V. S., Hornig, G., & Démoulin, P. 2002, *JGRA*, **107**, 1164
- Vaiana, G. G., Krieger, A. S., & Timothy, A. F. 1973, *SoPh*, **32**, 81
- van Driel-Gesztelyi, L., Hofmann, A., Demoulin, P., Schmieder, B., & Csepura, G. 1994, *SoPh*, **149**, 309
- Welsch, B. T., & Longcope, D. W. 1999, *ApJ*, **522**, 1117
- Winebarger, A. R., Warren, H. P., & Mariska, J. T. 2003, *ApJ*, **587**, 439
- Wright, A. N., & Berger, M. A. 1989, *JGR*, **94**, 1295